Investigating the discrepancy between wet-suspension and dry-dispersion derived ice nucleation efficiency of mineral particles

C. Emersic[1]**, P. J. Connolly**[1]**, S. Boult**[1]**, M. Campana**[2]**, and Z. Li**[2]

[1]School of Earth, Atmospheric and Environmental Sciences, The University of Manchester, UK
[2]School of Physics and Astronomy, The University of Manchester, UK

Correspondence to: P. J. Connolly (p.connolly@man.ac.uk)

Abstract

Cloud chamber investigations into ice nucleation by mineral particles were compared with results from cold stage droplet freezing experiments. Kaolinite, NX-illite, and K-feldspar were examined and K-feldspar was revealed to be the most ice active mineral particle sample, in agreement with recent cold stage studies. The ice nucleation efficiencies, as quantified using the *ice-active surface site density* method, were found to be in agreement with previous studies for the lower temperatures; however, at higher temperatures the efficiency was consistently higher than those inferred from cold stage experiments. Numerical process modelling of cloud formation during the experiments, using the cold-stage-derived parameterisations to initiate the ice phase, revealed the cold-stage-derived parameterisations to consistently under predict the number of ice crystals relative to that observed. We suggest the reason for the underestimation of ice in the model is that the slope of the cold-stage-derived *ice-active surface site density* vs temperature curves are too steep, which results in an underestimation of the number of ice crystals at higher temperatures during the expansion. These ice crystals suppress further freezing due to the Bergeron-Findeison process. Application of a coagulation model to the size distribution of mineral particles present in the suspensions as used in the cold-stage-derived parameterisations is used to investigate the idea that the mineral particles coagulate in suspension, which either removes the particles from the drops by sedimentation, whilst in the bulk suspension, or reduces the total particle surface area available for ice nucleation to take place. Aggregation is confirmed using dynamic light scattering measurements of colloidal suspensions. The implication is that the mineral particles may be more important at nucleating ice than previously thought at high temperatures.

1 Introduction

Recently Hiranuma et al. (2014) determined ice nucleation efficiency of the NX-illite dust sample using a variety of methods. The methods were broadly classed as "wet-suspension"

methods, where mineral particles were put into water suspension before droplets of the suspension were cooled and frozen, or "dry-dispersion" methods, where the mineral particles act as cloud condensation nuclei followed by freezing. Hiranuma et al. suggested that there was a discrepancy between the dry-dispersion methods and the wet-suspension methods at high temperatures, which they attributed to a change in chemical composition of the NX-illite mineral during dissolution in water. They also discussed the potential effect of agglomerates and posibility of multiple nucleation modes, and suggested that further work was needed to better understand instrumental limitations.

Atmospheric mineral dust particles are comprised of several different minerals (e.g. Glaccum and Prospero, 1980; Kandler et al., 2007) and it is possible to determine their ice nucleation activity (e.g. Connolly et al., 2009, and others). However, there is much to be learned by investigating the ice nucleating ability of less complex "pure minerals". Using a technique originally described by Vali (1971), Kaolinite (KGa-1b from the clay mineral society) and NX-illite have recently been examined in the immersion freezing nucleation mode (Murray et al., 2011; Broadley et al., 2012) and parameterisations of the ice-active surface site density have been put forward as have those for K-feldspar (Atkinson et al., 2013). These studies used "wet-suspensions" to investigate ice nucleation by immersion freezing. They quantified the ice nucleation ability of the pure minerals using the ice-active surface site density concept, described as the number of ice active sites per unit surface area of dust, n_s, as presented by Connolly et al. (2009).

Murray et al. (2011) showed that the number of ice active sites on dust scales with the total surface area of dust in a drop; however, the total surface area available in the droplets was relatively large due to high particle concentrations in the dust suspension used to generate the droplets. In some cases the number concentrations exceeded $10^{17}\,\mathrm{m^{-3}}$, which equates to an inter particle spacing of $\sim 2\,\mu\mathrm{m}$, if one assumes equal spacing between the particles. At these high particle concentrations one might expect some interaction between neighbouring particles if they are able to come together and adhere due to the van der Waals interaction.

3

In nature, it is unlikely such high dust concentrations will be present in supercooled cloud droplets. Hence, the aim of this paper is to use a combination of laboratory experiments, data analysis and modelling to reconcile two different approaches for determining ice nucleation efficiency.

2 Experimental set-up

Experiments were conducted in the Manchester Ice Cloud Chamber (MICC) fall tube, which has a diameter of 1 m and height of 10 m (additional details of the general facility are described in Connolly et al., 2012). The MICC and experimental set-up are shown in Fig. 1. Initially, the chamber was pressure sealed and evacuated using two scroll pumps, capable of reducing pressure at a rate of approximately 1.4 hPa s^{-1}, to 200 hPa before refilling with filtered air. The filtered air had 10–20 cm^{-3} < 5 nm particles, with a total particle mass concentration < 0.01 µg m^{-3}. Volatile Organic Carbon, VOC, measurements by the Leicester Proton Transfer Reaction Mass Spectrometer always indicated VOC levels below detection limits of approximately 1 ppb. This cleaning process was repeated a total of three times to reduce background aerosol concentration inside MICC to typically 20 cm^{-3}. The chamber was then cooled to the desired temperature, ranging from −12 to −27 °C depending on the experiment, and allowed to thermally equilibrate.

Prior to conducting the cloud formation experiments, a background experiment was performed in which the pressure was reduced to 700 hPa to check that the remaining background aerosol in the chamber post-cleaning were not ice nuclei. Ice was only ever observed in low concentrations of a few cm^{-3} at the lowest temperatures and was attributed to homogeneous nucleation when the temperature during the pressure reduction process approached −36 °C. In the case where this was observed, the ice crystal concentration was substantially lower than the resulting concentration in the later experiments where mineral dust particles were present.

Following the background experiment, a selected mineral dust was inserted into the chamber using a PALAS dust generator (RBG 1000 ID). This instrument uses particle free

4

compressed air to separate and insert dust particles from a rotating brush which collects them from a reservoir. The dust was inserted into the top of the chamber and allowed to homogenise; an initial measurement was taken using an Ultra High Sensitivity Aerosol Spectrometer (UHSAS), which uses an intracavity laser to measure aerosols in the size range (50–1000 nm) and a PALAS WELAS 2000 aerosol probe indicating total initial concentrations of approximately 1000–2000 cm^{-3}.

Liquid cloud drops formed as the pressure was reduced to 700 hPa from ice saturated conditions, and this was sampled with cloud probes, including the PALAS WELAS 2000 (WELAS), Droplet Measurement Technologies Cloud Droplet Probe (CDP), and the Stratton Park Engineering Company Cloud Particle Imager 3V (3V-CPI). Briefly, the WELAS infers the size of particles from the intensity of the light they scatter at 90°. The CDP operates on a similar principle to the WELAS, but uses a solid state laser (658 nm) and detects light scattered by particles ($3 < D < 50 \mu$m) in the forward direction (4-12°). The 3V-CPI takes images of particles ($20 < D < 2000 \mu$m), that pass through the sample volume, using a pulsed infrared laser incident on a CCD array. 3V-CPI images that are greater than 35 μm in length are analysed for their shape to determine if they are ice crystals or not. For these large shapes we are confident in discriminating between drops and ice crystals; hence, the remaining errors are due to Poisson counting.

Internal chamber pressure was measured using a Lex 1 Keller pressure probe and the air temperature was measured using calibrated type K thermocouples arranged along the height of and in the centre of the cloud chamber. Several repeat pressure reduction cycles were performed once dust was inserted; after each experiment, the chamber was filled back to ambient pressure using the clean air system described above. A set of experiments for each dust was performed at both higher and lower temperature, and in total, Kaolinite, Feldspar, and Illite were used, giving a total of 6 experiment sets comprising ~ 4 runs per set (a total of ~ 24 depressurisations, not including background runs).

3 Observations

Figures 2 and 3 show the results of the two first experimental runs on K-feldspar – the same sample used in the Atkinson et al. (2013) study. Figure 2 was conducted with the initial temperature equal to $-12\,^\circ$C and expansion of the air to 700 hPa resulted in the temperature decreasing to $\sim -19\,^\circ$C. The middle plot of Fig. 2 shows the time evolution of the measured size distribution from the CDP. Mineral particles are visible at the start of the experiment at sizes up to $\sim 10\,\mu$m, whereas ~ 25 s into the experiment a cloud of droplets grows as noted from the brighter colours. Following the formation of drops, ice crystals are formed and grow to large sizes.

The cloud of drops evaporates at ~ 200 s due to the Bergeron-Findeison process, following which the ice crystals are able to persist to ~ 300 s. The bottom plot of Fig. 2 shows that the drop concentration measured with the CDP reaches $\sim 2000\,\mathrm{cm}^{-3}$. The ice concentration determined by the 3V-CPI (red-line) agrees very well with the concentrations of particles greater than $20\,\mu$m as measured with the CDP (blue line), thus giving confidence in our measurements of ice crystal concentration. The blue-dashed line is the concentration of particles greater than $35\,\mu$m measured with the 3V-CPI. It should be noted the reason this is greater than the concentrations of particles greater than $20\,\mu$m measured with the CDP is because the 3V-CPI often over-sizes out of focus images of droplets (Connolly et al., 2007).

Figure 3 shows the results of the first run of K-feldspar at an initial temperature of $-21\,^\circ$C. During the expansion the air temperature reduced to $\sim -28\,^\circ$C. The CDP showed evidence of droplets forming for a brief period at ~ 40 s in to the experiment (middle plot and black line on bottom plot). However, the droplets lasted for a brief period (less than ~ 40 s). The 3V-CPI concentration is lower than the CDP concentration of particles greater than $20\,\mu$m (blue line); however, in this experiment it was difficult to discriminate the ice crystals on shape alone because the ice crystals appeared somewhat rounded due to the lack of vapour growth. Furthermore, the concentrations of particles greater than $20\,\mu$m, measured with the CDP, and those measured with the 3V-CPI greater than $35\,\mu$m are in good agreement. For

this experiment it was more accurate to use these two measurements for the ice crystal concentrations.

Similar plots are shown in Figs. 4 and 5, but for kaolinite at $-19\,°C$ and $-25\,°C$ respectively. In Fig. 4 (middle plot) a cloud of droplets forms for ~ 50 seconds before evaporating to leave an ice cloud. It is more difficult to see from the CDP data that the ice cloud nucleates after the drops form, because the optical sizes of the ice crystals overlap with the optical sizes of the largest kaolinite particles; nevertheless the 3V-CPI data indicated that this was the case (not shown). The bottom plot of Fig. 4 shows that the 3V-CPI derived ice crystal concentration (red line) is about a factor of two smaller than the particles larger than $20\,\mu m$ from the CDP (and those larger than $35\,\mu m$ from the 3V-CPI, blue lines); this is because some of the ice crystals are too small to be able to unequivocally classify them as ice crystals on their shape alone, so we slightly underestimate the ice concentration here.

Figure 5 middle shows that the kaolinite particles nucleate ice in the absence of a cloud of droplets. In fact, the droplets are too small to see with the CDP: the humidity in the chamber was close, and likely above water saturation. The drops are not visible because the Bergeron-Findeison process acts rapidly in this experiment, leaving the drops with little time to grow. The drop mode became more visible with repeat experiments (not shown): (a) because the particle concentration was diluted and (b) because the largest, most IN active particles were used up, which enabled the drops to grow to larger sizes. As for the experiment at higher temperature the 3V-CPI derived ice crystal concentration was below that of the concentrations that were derived on size alone from the CDP and 3V-CPI (solid blue and dashed blue lines respectively). Again this is because the particle sizes were often too small to unequivocally classify them as ice; hence, we classified the ice based on size for these runs (blue lines).

Finally, we have similar plots for the NX-illite sample in Figs. 6 and 7. In Fig. 6 (top) we see that the initial temperature was $-15\,°C$, which decreased to $\sim -23\,°C$ throughout the experiment. The middle plot shows that the droplet mode was of fairly long duration, lasting up to $\sim 300\,s$ and that there were relatively few ice crystals (as noted from the few speckles above $20\,\mu m$ in size). The 3V-CPI and CDP derived ice concentrations agree reasonably

well in this case; however, the concentration of particles larger than 35 µm as measured with the 3V-CPI is larger than those larger than 20 µm measured with the CDP. The reason for this is that the 3V-CPI has a tendency to over estimate the size of the drops when they are out of focus. Drop concentrations were $\sim 2000\,cm^{-3}$.

For NX-illite at $-25\,°C$ in Fig. 7 the picture is similar to K-feldspar and kaolinite at the lower temperatures. There is no visible drop mode and the ice crystal concentration inferred from the 3V-CPI images is lower than those inferred from the CDP and 3V-CPI on size alone (bottom plot). The drop mode was visible in later expansions, when the most efficient ice nuclei had been used up and thus removed from the chamber (not shown). The reason the 3V-CPI derived ice crystal concentrations were smaller than the CDP and 3V-CPI concentrations based on size is again due to the ice crystals not developing distinct facets because there are many of them; hence, for these experiments we classified the ice on size alone (blue lines). It is noteworthy that drop concentrations were $\sim 500\,cm^{-3}$, which is lower than the aerosol by a factor of ~ 3. We suspect that NX-illite, because of its high specific surface area and heteorgeneity, is less effective as a cloud condensation nucleus (CCN) than the other samples, which may be explained by NX-illite having a different adsorption isotherm (e.g. Kumar et al., 2008) in comparison to the other samples.

4 Analysis

To compare our dry dispersion chamber observations with wet suspension cold stage methods (e.g. Murray et al., 2011; Broadley et al., 2012; Atkinson et al., 2013) we used two main approaches. Firstly we calculated values of the ice-active surface site density, or n_s, using our data and plotted them on the same graph as existing data taken using cold stages (see Sect. 4.1). Secondly the Aerosol-Cloud-Interactions Model (ACPIM) (Connolly et al., 2012) was used to simulate the MICC cloud chamber experiments. In this model, the freezing parameterisations of Murray et al. (2011); Broadley et al. (2012); Atkinson et al. (2013) have been implemented and were used to compare ice concentrations expected with those observed. ACPIM is discussed and the analysis is presented in Sect. 4.2.1.

4.1 Calculating n_s directly from the data

We calculated n_s directly from the data in the following way. The result of the n_s concept is that the fraction of drops, f, containing surface area, A, that are frozen at temperature, T, is described by the factor:

$$f = 1 - \exp\left(-A n_s[T]\right) \tag{1}$$

Hence, for an input dust particle size distribution, $\frac{dN}{dD}$, where all particles are hygroscopic, or take up at least a mono-layer of water, we write the number of ice crystals that are nucleated as:

$$N_{\text{ice}} = \int_{D_{\text{min}}}^{D_{\text{max}}} \frac{dN(D)}{dD} \left(1 - \exp\left(-A n_s[T]\right)\right) dD \tag{2}$$

Here D_{min} and D_{max} are the minimum and maximum particle size in the mineral particle size distribution.

The value used for A in Eq. (2) is the surface area of a sphere multiplied by a factor to yield the BET specific surface area (see Table 3). We calculate n_s iteratively using data and Eq. (2). Firstly, we use an initial guess of n_s and evaluate the integral in Eq. (2). We then compare the calculated value of N_{ice} with the measured value. This process is repeated with updates to n_s until the integral is equal to N_{ice}, at which point the method has converged.

Another way of estimating n_s (e.g. Niemand et al., 2012; Hiranuma et al., 2014) has been to divide the measured ice crystal number concentration by the surface area of the aerosol size distribution, as measured at the start of the experiment (with a pressure correction for dilution during the expansion):

$$n_s \cong \frac{N_{\text{ice}}}{\pi \int_{D_{\text{min}}}^{D_{\text{max}}} D^2 \frac{dN(D)}{dD} dD} \tag{3}$$

However, this method can lead to an underestimation of n_s because it does not take into account the removal of surface area from the dust size distribution as they nucleate ice.

The values of n_s derived using the iterative method are shown in Fig. 8. We have chosen to plot each experimental run as a single data point. Note that the spread in n_s values, for data points that are close together in temperature, arises because experiments were repeated for several expansions, which allowed the most efficient ice nuclei to be depleted from subsequent expansions. Since the ice crystal concentrations are measured with time we could use a single experiment for multiple data points as is typically done in other studies (e.g. Niemand et al., 2012; Hiranuma et al., 2014); however, we have more confidence in the accuracy of the experimentally averaged data points. It can be seen that at the higher temperatures, values from the chamber (using dry dispersion) are significantly larger than those taken from cold stages (using wet suspension). This effect has been noted for NX-illte in the recent study by Hiranuma et al. (2014).

4.2 Process modelling

The application of ACPIM to understand and interpret the implications observations is described in Sect. 4.2.1, below. The discrepancies noted in Fig. 8 prompted us to understand the reason for differences between dry-dispersion and wet-suspension techniques; hence, coagulation model calculations are presented in Sect. 4.2.2.

4.2.1 Chamber modelling

We operated ACPIM as a cloud parcel model with bin microphysics. The aerosol size distributions were specified as lognormal fits to the observed data from the UHSAS and the WELAS probes (see Table 1). The curves were manually fitted to the data. Since the background aerosol were not ice nuclei we assumed they were hygroscopic aerosol (ammonium sulphate). A single lognormal mode of ammonium sulphate aerosol was used to describe the background aerosol measured during the background experiment while two lognormal modes were used to describe the mineral particle size distribution that was measured prior to the experiment. The background aerosol could be clearly distinguished from the mineral particle size distribution by size: the background distribution was narrow and had a median

diameter of $\sim 40\,\text{nm}$; whereas the mineral particle distribution was broad and had a median diameter of $\sim 400\,\text{nm}$. It was assumed that the mineral dust had a small amount of soluble material on them, to enable them to act as cloud condensation nuclei (as well as ice nuclei). The model was relatively insensitive to the fraction of soluble material assumed in the range 1–5 % (by mass). The parcel model was forced with the observed pressure drop rate and the temperature rate of change was calculated from the conservation of energy (1st law of thermodynamics) for moist air with the addition of a first order derivative that depends on the temperature difference between the gas and the chamber walls. In the model, total water content remained constant during an experiment (which was consistent with the condensed mass inferred from the CDP measurements and water vapour concentration measured by a tunable diode laser).

The condensation process was described by the droplet growth equation (Pruppacher and Klett, 1997), with equilibrium vapour pressures described by Köhler theory. Ice nucleation was modelled using the parameterisation of Koop et al. (2000) for homogeneous freezing or, Murray et al. (2011); Broadley et al. (2012); Atkinson et al. (2013) for heterogeneous freezing by the kaolinite, illite or feldspar mineral dust respectively. A criteria was added that a dust particle had to have 5×10^{-14} kg of water condensed before it could act in the immersion / condensation mode – this prevented ice nucleation at conditions that were sub-saturated with respect to water, as observed. Once nucleated ice crystals grew according to the ice crystal growth equation (Pruppacher and Klett, 1997), and in this work crystals were assumed to be quasi-spherical with a variable effective density (see Connolly et al., 2012, for details). All derivatives form a large set of coupled ODEs, which were solved using the DVODE solver from Netlib.

The ACPIM model was run for every experiment in Table 1 and the results are summarised as ratios of observed to simulated ice crystal concentrations in Fig. 9. The statistics in Fig. 9 were calculated from each of the experimental runs for a particular set of experiments. In general it is shown that the parameterisations underestimate the ice crystal concentrations at all temperatures whereas from Fig. 8 one would expect the parameterisations to do reasonably well at the lower temperatures. The reason the parameterisations do

11

not do well at low temperatures is because the dry dispersion data suggest that the slope of the n_s vs temperatures curves should be shallower, thus yielding higher values of n_s at the start of the expansion.

4.2.2 Coagulation modelling

In the experimental approaches relying on wet suspension, mineral particles are added to a large volume of water and the wet suspension is stirred for ~ 12 hours with a magnetic stirrer. The drops containing mineral particles in suspension are then either sprayed (in which case pico-litre drops are produced) or pipetted onto a glass slide (in which case micro-litre drops are produced). A few minutes may then elapse before commencing the cooling of drops. Hence, it is possible that coagulation of particles happens, either in the large volume of water, or in the drops before and during the cooling cycle.

We modelled the coagulation of particles within wet-suspensions using the model described in Appendix A. We present the results here neglecting the electric double charge layer that is commonly used to describe inter-particle forces in a colloid (our justification for this is discussed in Sect. 5.1.1).

Simulations with the coagulation model were performed for 2 h run-time. We performed simulations for two weight percents (0.005 and 1.000) and also used 3 assumptions for the size of the water drops that the mineral particles were suspended in. The first was to assume a pico-litre volume drop (1×10^{-15} m^3); the second was to assume a micro-litre volume drop (1×10^{-9} m^3) and the third was to assume an infinite volume of water. The reason for these choices was that they span the range of conditions encountered in the cold stage experiments. We also used different coagulation kernels: one where forces due to Brownian motion were the only forces governing the motion of the particles; and another where Brownian and gravitational settling forces were acting.

Figure 10 shows results from the coagulation model assuming that the forces governing the movement of mineral particles are those due to Brownian motion only. Figure 10a and b show that hardly any coagulation occurs within the pico-drops at the weight percents assumed in the calculations. This is evident from the fact that the particle sizes do not

change with time. There are just too few particles present for coagulation to be efficient. When micro-litre drops are used (Fig. 10c and d) we see that the size of the mode shifts to larger sizes. This is significant for the larger weight percent drops where the median size shifts from sub-micron to 10 s of microns. The assumption of an infinite volume of water in Fig. 10e and f yields similar results to the micro-litre model run.

From the results in Fig. 10 we have calculated the ratio of mineral particle surface area to the initial mineral particle surface area. These calculations are shown in Fig. 11. We have assumed that a collision between two mineral particles yields a mineral particle with the same volume as the other two and that they produce quasi-spherical particles with a fractal dimension of ~ 2 (as shown by, Vaezi G et al., 2011). Figure 11 shows that, at the highest weight percent in the micro-litre drop, the surface area of the mineral particles quickly drops to ~ 0.1 of the initial value. For the highest weight percent in the pico-litre drop and for the lowest weight percent of the micro-litre drop we see that the surface area available for nucleation is ~ 0.5 of the initial value. Finally, for the lowest weight percent in the pico-litre drop we see no reduction in the available surface area.

Figure 12 shows the same calculation of available surface area vs. time when both Brownian motion and gravitational settling influence the coagulation kernel. Similar results to those for the Brownian only kernel are shown for the pico-litre drops and also for the micro-litre at low weight percent; however, for the micro-litre drop at high weight percent we see that the available surface area quickly drops to 0.005 of the initial value. This is in the region required to explain the discrepancies seen in Fig. 8.

It should be noted that our simulations of coagulation offer a rough calculation of the reduction in surface area due to coagulation. However, another important process to consider is the fact that, once aggregated, large particles will sediment out of the suspension; therefore further reducing the available surface area for nucleation. The subsequent calculations of n_s will be biased low because the surface area used to calculate n_s (the original surface area added to the suspension) will be too high.

4.3 Colloid experiments

In order to support our calculations we have conducted experiments where we prepare colloidal suspensions at 0.1 to 1 wt % solids (either K-feldspar, kaolinite or nx-illite) in ultrapure (18.2 MΩ cm) water.

We stirred the suspensions for 12 h using a magnetic stirrer to reproduce the methods of previous ice nucleation studies and then passed them through either 1 μm or 5 μm filters (22 mm Cellulose nitrate membrane, Whatman, UK). We found in all cases that this process reduced the absorbance of UV and visible light to that of ultrapure water (UV-Vis spectrometer, Stellarnet, Fla., USA) and, therefore, removed the particles completely to within error of the absorbance measurements. Less than 2 ml of suspension was passed through the filter membranes and their effective pore-size would have remained unaltered. This, therefore, suggests that the particles had aggregated from their initial sub-micron sizes to super micron sizes. We also monitored the absorbance of the suspension vs time across the spectrum; at 567 nm, the optimum wavelength with respect to signal to noise, and found it to decrease by a factor of 10 within 90 min of sample preparation. This also suggests that sedimentation and aggregation had occurred.

Measurements were performed using a Malvern Zetasizer Nano ZS at the University of Manchester, UK. Kaolinite suspensions were prepared (MilliQ H2O and 100 mM NaCl) to study the effect of electrolytes on particle aggregation. The water was filtered with a 0.2 μm PTFE filter to eliminate possible dust particles. Measurements of the kaolinite samples were conducted with concentrations of 0.1, 0.33 and 1 mg ml^{-1} (0.01, 0.033 and 0.1 wt %) prepared by mild sonication for 5 min at 60 °C then immediately cooled to room temperature and measured within minutes. Note that in the absence of heating to 60 °C the particles remained in an aggregated state. The pH was varied between 3 and 11 by addition of the minimum amount of diluted HCl or NaOH, respectively and the results are summarised in Table 2.

Measurements in MilliQ water show an increase in particle size with increasing kaolinite concentration. It is notable that at pH ∼ 9.0 there is a factor of two increase in particle size

14

going from $0.33\,\mathrm{mg\,ml^{-1}}$ concentration to $1\,\mathrm{mg\,ml^{-1}}$ since the pH of kaolinite in MilliQ water was measured to be ~ 8.2 in the aggregated sample; thus suggesting that aggregation is important. The effect of electrolytes is clearly seen in the lower half of Table 2. At high NaCl concentrations aggregation is enhanced, as expected, since charges on the clay minerals are neutralized by the mobile charges in solution. It is not clear whether this enhancement in aggregation is due to a reduction in like-like charge repulsion or an enhancement in the attraction of particles with different zeta-potential in the heterogeneous mineral particle sample (see Appendix C, Fig. 13).

5 Discussion

Recently Hiranuma et al. (2014) suggested that there is a discrepancy between the dry-dispersion and wet-suspension methods of determining the ice nucleation efficiency of the clay mineral NX-illite. They explained that the mineral surface is chemically altered during reaction with water, which may affect the ice nucleating activity. Their measurements of ion concentrations in water containing NX-illite supported this finding; however, since ion concentrations are able to screen surface charge on colloidal particles these charges may significantly enhance the ability of the particles to coagulate (see Appendix B and C). We also confirm that the dry-dispersion method we used predicts higher values of n_s than the previously published results using wet-suspensions at high temperatures, but that the two methods are in close agreement at the lower temperatures. We offer an alternate explanation to that of Hiranuma et al. (2014), which is that the mineral particles may coagulate together in suspension and reduce the surface area available for nucleation.

This explanation is also consistent with the discrepancy found at high temperatures: in the wet-suspension methods, the high temperature results use the highest mineral particle weight percents, which are more likely to coagulate. However, Atkinson et al. (2013) show that high weight percents (0.8 %) in pico-litre drops at lower temperatures that agree with our dry-dispersion measurements. We suggest a possible reason is that the K-feldspar particles form relatively weak aggregates, which can be disrupted and broken up by energetic

15

spraying into pico-litre size drops, but not by pipetting into micro-litre drops. This may explain (with reference to Fig. 12) why the pico-litre drops at high weight percent presented in Atkinson et al. (2013) agrees with our measurements, but the micro-litre drops at the same weight percent do not. Coagulation can also occur within micro-litre drops, but tends not to in pico litre drops because they lack sufficient mineral particles for the process to be efficient. Another alternate explanation is that the spraying process for the pico-litre drops causes the aggregates to be disrupted.

5.1 Does the assumption of spherical particles affect our findings?

We note that Fig. 8 is adjusted so that we take account of the specific surface area; however, the process modelling (Fig. 9) assumes the surface area of spherical mineral particles. Here we assess whether this affects the main findings. The quoted values for BET specific surface areas of the three samples are shown in Table 3.

We estimate the discrepancy in the assumption that the particles are spherical. The median diameter for the three samples when introduced into the chamber was approximately $D_m = 0.4 \times 10^{-6}$ m. The calculated surface area to mass ratio is then, S:

$$S = \frac{6D_m^{\cancel{2}}}{\rho D_m^{\cancel{3}}} \tag{4}$$

$$= \frac{6}{\rho D_m} \tag{5}$$

We may then calculate the SSA underestimation factor, which is the ratio of the SSA to the value of S. Table 3 shows that the assumption of spherical particles likely underestimates the surface area for the kaolinite and NX-illite samples by factors of ~ 2 and ~ 20 respectively. For the K-feldspar the assumption of sphericity overestimates the surface area by a factor of ~ 2. The underestimation is because the particles are platelets so measured optical size is closer to $\frac{\pi D^2}{2}$ (area of a disk) instead of πD^2 (area of a sphere). It should be noted that these values are not large enough to significantly affect the conclusions from Fig. 9.

16

5.1.1 Colloidal forces in suspensions

The coagulation modelling in Sect. 4.2.2 neglected the force of repulsion due to the electric double charge layer (see Appendix B and C for details). Kaolinite is a 1:1 layer clay consisting of alternating silca (tetrahedral) and alumina (octahedral) layers, which are bonded together. The tetrahedral faces have a net negative charge due to isomorphic substitution of silicon ions by ions with a lower charge, whereas the edges and octahedral faces have charges that depend on the pH of the solution.

When placed in suspension the minerals develop a double charge layer by attracting positive ions (counter-ions) to the surface. The double charge layer can result in the particles being colloidally stable because of the effective like-charge Coulomb interaction between two particles. The sign and magnitude of the charge layer can be quantified by inferring the zeta-potential from measurements of electro-phoresis.

We now provide some justification for the decision to neglect it. Elimelech et al. (2000) have shown that the ζ-potential is a relatively insignificant factor in predicting the transport / sedimentation of particles when there is heterogeneity in the surface of the colloidal material. This is reasonable since the ζ-potential is only a bulk measurement of the charge on a population of particles.

Tombácz and Szekeres (2006) have since shown that kaolinite has surface charge heterogeneity due to the mineral having permanent charges on the tetrahedral silica faces and pH dependent charges on the crystal edges and also the octahedral alumina faces. In the paper by Tombácz and Szekeres (2006), kaolinite samples were heavily processed to remove the large particle sizes and any other contamination; however, surface charge heterogeneity still persisted.

The faces of alumina and edges of the kaolinite crystal may undergo hydrolysis and hence carry pH dependent charges (Tombácz and Szekeres, 2006). Tombácz and Szekeres (2006, their Fig. 7) show that, at pH 7, these alumina and silica groups (as inferred through a linear combination of their zeta potential) may have an overall charge close to zero. Hence, there is surface charge heterogeneity in clay minerals. Indeed Schofield and Samson (1954)

17

had noted previously that "edge to face" coagulation (or flocculation) occurs in kaolinite samples.

Berka and Rice (2005) have shown that kaolinite can be colloidally stabilized at particle concentrations similar to those under consideration here ($\sim 10^{16}$ m^{-3}); however, their results are at pH of 9.5, where the alumina also carries high negative charge; hence, it should be expected that kaolinite will be colloidally stabilized to some extent at pH 9.5. Our own dynamic light scattering measurements confirm that high pH does cause some colloidal stability, but that this can be overcome at higher concentrations (Table 2).

6 Conclusions

Experiments were conducted in the Manchester Ice Cloud Chamber facility to look at ice nucleation in the condensation mode. Three dusts were investigated: kaolinite, illite, and feldspar, and each dust was examined at relatively high and low temperatures. The primary goal of this study was to reconcile dry-dispersion methods of quantifying ice nucleation on mineral dusts with those using wet-suspension.

Observations revealed feldspar to be the most efficient dust at nucleating ice (Fig. 8) in agreement with Atkinson et al. (2013), followed by illite, then kaolinite. Thus our data are qualitatively in agreement with previous findings. However, they all showed a discrepancy at the higher temperatures; the dry dispersion methods always showed higher values of n_s than the wet-suspension methods.

Using the ACPIM numerical model to simulate the cloud chamber with ice nucleation parameterisations provided by Murray et al. (2011); Broadley et al. (2012), ice concentrations for all dusts were underestimated relative to observations. The reason for this was that the slope of the n_s vs. temperature curves were determined to be less steep in our measurements than the wet-suspension methods. Hence, the reason the model under-predicted the ice crystal concentration at lower temperatures was because the values of n_s from the parameterisations were too low at the start of the experiment. Thus too few ice crystals were

nucleated and by the time the lower temperatures were reached the Bergeron–Findeison process had led to the evaporation of the drops.

Modelling of coagulation in suspension showed that it may be a pathway to significantly reduce the surface area of mineral particles and hence would reduce the effective n_s calculated from experimental data. This is confirmed by separate experiments passing the suspensions through filters after initial dispersion and also through dynamic light scattering.

To explain the discrepancy between dry-dispersions and wet-suspensions we suggest the following:

– During the stirring process feldspar particles do not adhere strongly to each other. These weak aggregates may thus be easily disrupted when pico litre drops of the suspension are sprayed, because the drops are a similar size to the aggregate particles in this case.

– Illite and kaolinite particles form stronger, more tightly packed, aggregates and could sediment during the stirring process.

– At high concentrations ~ 1.000 wt % coagulation is more likely to happen.

– As the drops are either sprayed, or pipetted onto the glass slide the mineral particles within the drops may start to coagulate.

– After generation of the pico-litre drops they contain insufficient mineral particles, even at 1.000 wt %, to result in significant coagulation.

– In micro-litre drops there are enough mineral particles to result in significant coagulation, and a reduction of surface area in the drops. This reduction increases with increasing wt % of mineral particles.

– The slopes of the n_s vs temperature derived from our dry dispersion experiments more closely agree with those derived for natural dusts by Niemand et al. (2012).

– The dry-dispersion techniques suggest that mineral particles are more efficient than the wet-suspension derived parameterisations suggest, especially at relatively high temperatures.

Appendix A: Modelling coagulation in suspension

We adopted the semi-implicit numerical algorithm for treating the coagulation process (pp 438 Jacobson, 1999). This method conserves total particle volume and approximately conserves the monomer concentration. The algorithm is written as follows:

$$v_{k,t} = \frac{v_{k,t-1} + dt \sum_{j=1}^{k} \left(\sum_{i=1}^{k-1} f_{i,j,k} \beta_{i,j} v_{i,t} n_{j,t-1} \right)}{1 + dt \sum_{j=1}^{N_B} (1 - f_{k,j,k}) \beta_{k,j} n_{j,t-1}} \tag{A1}$$

with $n_k = \frac{v_k}{\nu_k}$ and:

$$f_{i,j,k} = \begin{cases} \left(\frac{\nu_{k+1} - V_{i,j}}{\nu_{k+1} - \nu_k} \right) \frac{\nu_k}{V_{i,j}} & \nu_k \leq V_{i,j} < \nu_{k+1} \text{ if } k < N_B \\ 1 - f_{i,j,k-1} & \nu_{k-1} < V_{i,j} < \nu_k \text{ if } k > 1 \\ 1 & V_{i,j} \geq \nu_k \text{ if } k = N_B \\ 0 & \text{all other cases} \end{cases} \tag{A2}$$

Equation (A1) shows that the solution at the next time-step depends on the solution at that time-step; hence, the method is an "implicit" method; however, the algorithm is solve sequentially in discrete bins such that the solution at the next time-step is always known.

The variable β is the coagulation kernel of two interacting particles (m^3 particle^{-1} s^{-1}). When by the concentration of particles in a discrete bin it gives the rate of the number of particle interactions. We assume it can be described by the sum of a kernel due to Brownian diffusion and that due to gravitational settling. For Brownian the diffusion the kernel takes

the form:

$$\beta(i,j) = 4\pi \left(r_i + r_j\right)\left(D_{\mathsf{p},i} + D_{\mathsf{p},j}\right) \tag{A3}$$

where $D_{\mathsf{p},i}$ and $D_{\mathsf{p},j}$ are particle diffusion coefficients:

$$D_{\mathsf{p},i} = \frac{k_{\mathsf{B}}T}{6\pi r_i \eta_{\mathsf{w}}} \tag{A4}$$

following Einstein (1956). This model assumes that each Brownian collision results in a sticking event.

For gravitational settling the kernel takes the form:

$$\beta(i,j) = E_{i,j}\pi \left(r_i + r_j\right)^2 |u_{t,i} - u_{t,j}| \tag{A5}$$

Appendix B: Interaction potential of minerals in suspension

A particle suspended in water will generally form a double charge layer by accumulation of ions.

The potential energy of the electrical double layer interaction between two spheres may be written:

$$V_R = \left(\frac{\pi\epsilon R_1 R_2}{R_1 + R_2}\right)(\zeta_1^2 + \zeta_2^2)\left(\frac{2\zeta_1\zeta_2}{\zeta_1^2 + \zeta_2^2}p + q\right) \tag{B1}$$

where R_1 and R_2 are the radii of the two interacting particles; ϵ is the electric permittivity; $\zeta_{1,2}$ are the zeta potentials of the interacting particles.

$$p = \ln\left(\frac{1 + \exp(-\kappa x)}{1 - \exp(-\kappa x)}\right) \tag{B2}$$

$$q = \ln(1 - \exp(-2\kappa x)) \tag{B3}$$

where x is the shortest distance between to particles and κ^{-1} is the Debye length:

$$\kappa^{-1} = \sqrt{\frac{\epsilon k_B T}{N_A e^2 \sum Z^2 m_i}} \tag{B4}$$

where k_B is Boltzmann's constant; N_A is Avogadros' number, $e = 1.6 \times 10^{-19}$ C is the charge on an electron; Z and m_i are the valence and molar concentration (moles per cubic metre) of ions; and T is the temperature.

In addition to the electrical double layer potential we also consider the van der Waals interaction, which is given by London's equation:

$$
\begin{aligned}
V_A = -\frac{A_{132}}{6}\Bigg(&\frac{2R_1 R_2}{[R_1 + R_2 + x]^2 + [R_1 + R_2]^2} \\
&+ \frac{2R_1 R_2}{[R_1 + R_2 + x]^2 + [R_1 - R_2]^2} \\
&+ \ln\left[\frac{[R_1 + R_2 + x]^2 + [R_1 + R_2]^2}{[R_1 + R_2 + x]^2 + [R_1 - R_2]^2}\right]\Bigg)
\end{aligned}
\tag{B5}
$$

here, A_{132} is the Hamaker constant for interaction between particle 1, particle 2 in medium 3. Individual Hamaker constants are as follows: for mineral particles we use A_1 and $A_2 =$

6.8×10^{-19} J; whereas for pure water we use $A_3 = 7 \times 10^{-21}$ J. A_{132} can be estimated (source) from the Hamaker constants for pure components:

$$A_{132} \cong \left(\sqrt{A_1} - \sqrt{A_3} \right) \left(\sqrt{A_2} - \sqrt{A_3} \right) \tag{B6}$$

The total potential for the interaction is given by the sum of van der Waals and the double electric charge layer: $V_T = V_A + V_R$.

Appendix C: Coagulation kernel with interaction potential

As described in Housiadas and Drossinos (2005, Sect. 6.3.1.2) the coagulation kernel can be corrected for the effect of an external, conservative force field. Here, "external" refers to the force field being external to the process considered in the uncorrected kernel. The correction is to divide the kernel by the factor:

$$Q = (R_i + R_j) \int\limits_0^\infty \frac{\exp\left[\frac{V_T(x)}{k_B T} \right]}{x^2} d_x \tag{C1}$$

We define the enhancement factor over the Brownian kernel, W, as the ratio of Q calculated with the interaction potential in Eqs. (B1) and (B5) to that calculated by van der Waals alone (B5). This enhancement factor is shown in Fig. 13 for two, spherical, $0.1\,\mu m$ diameter, particles having different values of the zeta-potential.

Figure 13 shows that two particles may come together if the zeta-potential of one of the particles has a magnitude less than a threshold of $\sim 10\,mV$. However, mineral particles are not spheres and exhibit patch-wise heterogeneity in their surface potential (see Sect. 5.1.1). Hence, we argue that for measured bulk zeta-potentials of $-20\,mV$ there may be enough heterogeneity in the sample, in addition to patch-wise heterogeneity, to lead to colloidal instability.

In addition Fig. 13 also shows that the enhancement factor may be greater than unity even when the particles have like change. This is seen most clearly at values of $\zeta_1 \cong -20\,mV$ and $\zeta_2 \cong 0\,mV$, where the enhancement factor is ~ 5. This behaviour is because the interaction between the two spheres produces induced charges, and has been observed experimentally in other studies.

References

Atkinson, J. D., Murray, B. J., Woodhouse, M. T., Whale, T. F., Baustian, K. J., Carslaw, K. S., Dobbie, S., O'Sullivan, D., and Malkin, T. L.: The importance of feldspar for ice nucleation by mineral dust in mixed-phase clouds, Nature, 498, 355–358, 2013.

Berka, M. and Rice, J. a.: Relation between aggregation kinetics and the structure of kaolinite aggregates., Langmuir, 21, 1223–1229, doi:10.1021/la0478853, 2005.

Broadley, S. L., Murray, B. J., Herbert, R. J., Atkinson, J. D., Dobbie, S., Malkin, T. L., Condliffe, E., and Neve, L.: Immersion mode heterogeneous ice nucleation by an illite rich powder representative of atmospheric mineral dust, Atmos. Chem. Phys., 12, 287–307, doi:10.5194/acp-12-287-2012, 2012.

Connolly, P. J., Flynn, M. J., Ulanowski, Z., Choularton, T. W., Gallagher, M. W., and Bower, K. N.: Calibration of the Cloud Particle Imager Probes using calibration beads and Ice Crystal Analogs: The depth-of-field, J. Atmos. Ocean. Tech., 24, 1860–1879, 2007.

Connolly, P. J., Möhler, O., Field, P. R., Saathoff, H., Burgess, R., Choularton, T., and Gallagher, M.: Studies of heterogeneous freezing by three different desert dust samples, Atmos. Chem. Phys., 9, 2805–2824, doi:10.5194/acp-9-2805-2009, 2009.

Connolly, P. J., Emersic, C., and Field, P. R.: A laboratory investigation into the aggregation efficiency of small ice crystals, Atmos. Chem. Phys., 12, 2055–2076, doi:10.5194/acp-12-2055-2012, 2012.

24

Einstein, A.: Investigations on the Theory of the Brownian Movement, Dover publications, New York, United States, 1956.

Elimelech, M., Nagai, M., Ko, C.-H., and Ryan, J. N.: Relative insignificance of mineral grain zeta potential to colloid transport in geochemically heterogeneous porous media, Environ. Sci. Technol., 34, 2143–2148, 2000.

Glaccum, R. A. and Prospero, J. M.: Saharan aerosol over the tropical north atlantic – mineralogy, Mar. Geol., 37, 295–321, 1980.

Hiranuma, N., Augustin-Bauditz, S., Bingemer, H., Budke, C., Curtius, J., Danielczok, A., Diehl, K., Dreischmeier, K., Ebert, M., Frank, F., Hoffmann, N., Kandler, K., Kiselev, A., Koop, T., Leisner, T., Möhler, O., Nillius, B., Peckhaus, A., Rose, D., Weinbruch, S., Wex, H., Boose, Y., DeMott, P. J., Hader, J. D., Hill, T. C. J., Kanji, Z. A., Kulkarni, G., Levin, E. J. T., McCluskey, C. S., Murakami, M., Murray, B. J., Niedermeier, D., Petters, M. D., O'Sullivan, D., Saito, A., Schill, G. P., Tajiri, T., Tolbert, M. A., Welti, A., Whale, T. F., Wright, T. P., and Yamashita, K.: A comprehensive laboratory study on the immersion freezing behavior of illite NX particles: a comparison of seventeen ice nucleation measurement techniques, Atmos. Chem. Phys. Discuss., 14, 22045–22116, doi:10.5194/acpd-14-22045-2014, 2014.

Housiadas, C. and Drossinos, Y.: Multiphase Flow Handbook, edited by: Clayton T. Crowe, CRC-Press, 6-1 -6-58, ISBN 9780849312809, http://www.crcnetbase.com/isbn/9781420040470, Sep 2005.

Jacobson, M. Z.: Fundamentals of Atmospheric Modelling, Cambridge University Press, Cambridge, UK, 1999.

Kandler, K., Benker, N., Bundke, U., Cuevas, E., Ebert, M., Knippertz, P., Rodriguez, S., Schutz, L., and Weinbruch, S.: Chemical composition and complex refractive index of Saharan mineral dust at Izana, Tenerife (Spain) derived by electron microscopy, Atmos. Environ., 41, 8058–8074, doi:10.1016/j.atmosenv.2007.06.047, 2007.

Koop, T., Luo, B., Tsias, A., and Peter, T.: Water activity as the determinant for homogeneous ice nucleation in aqueous solutions, Nature, 406, 611–614, 2000.

Kumar, P., Sokolik, I. N., and Nenes, A.: Parameterization of cloud droplet formation for global and regional models: including adsorption activation from insoluble CCN, Atmos. Chem. Phys., 9, 2517–2532, doi:10.5194/acp-9-2517-2009, 2009.

Murray, B. J., Broadley, S. L., Wilson, T. W., Atkinson, J. D., and Wills, R. H.: Heterogeneous freezing of water droplets containing kaolinite particles, Atmos. Chem. Phys., 11, 4191–4207, doi:10.5194/acp-11-4191-2011, 2011.

Niemand, M., Möhler, O., Vogel, B., Vogel, H., Hoose, C., Connolly, P. J., Klein, H., Bingemer, H., DeMott, P. J., Skotzki, J., and Leisner, T.: A particle-surface-area-based parameterisation of immersion freezing on mineral dust particles, J. Atmos. Sci., 69, 2012.

Pruppacher, H. R. and Klett, J. D.: Microphysics of Clouds and Precipitation, Kluwer Academic Press, Norwell, 1997.

Schofield, R. K. and Samson, H. R.: Flocculation of kaolinite due to the attraction of oppositely charged crystal faces, Discuss. Faraday Soc., 18, 135–145, doi:10.1039/DF9541800135, 1954.

Tombácz, E. and Szekeres, M.: Surface charge heterogeneity of kaolinite in aqueous suspension in comparison with montmorillonite, Appl. Clay Sci., 34, 105–124, doi:10.1016/j.clay.2006.05.009, 2006.

Vaezi G, F., Sanders, R. S., and Masliyah, J. H.: Flocculation kinetics and aggregate structure of kaolinite mixtures in laminar tube flow, J. Colloid Interf. Sci., 355, 96–105, doi:10.1016/j.jcis.2010.11.068, 2011.

Vali, G.: Supercooling of water and nucleation of ice (drop freezer), Am. J. Phys., 39, 1125–1128, 1971.

Table 1. Table showing summary of experimental results. Ice crystal concentrations are determined from the CPI number concentration of ice crystals, unless stated otherwise. Multiple rows indicate the expansion number on the same mineral particle sample after refilling to 1000 hPa. Geometric surface areas were obtained through integration of the size distribution assuming spherical particles. Errors in ice crystal concentration are calculating using Poisson counting statistics at the 0.05 level of significance.

Mineral sample	ice conc. (cm^{-3})	N (cm^{-3})	D_m (µm)	$\ln \sigma_g$	Geometric surface area (m^{-1})
K-feldspar @ $-12\,°$C	8.96 ± 0.15	[1700, 45]	[0.32, 2.8]	[0.3, 0.55]	1.99×10^{-3}
	6.31 ± 0.13	[1200, 15]	[0.32, 2.8]	[0.5, 0.55]	1.25×10^{-3}
	4.53 ± 0.11	[800, 4]	[0.32, 2.8]	[0.5, 0.45]	5.75×10^{-4}
	2.56 ± 0.08	[400, 3]	[0.32, 2.8]	[0.5, 0.65]	3.44×10^{-4}
K-feldspar @ $-21\,°$C [a]	47.16 ± 0.35	[1000, 20]	[0.32, 2.8]	[0.5, 0.8]	1.41×10^{-3}
	53.39 ± 0.38	[600, 20]	[0.33, 1.0]	[0.45, 1.5]	7.03×10^{-4}
	32.56 ± 0.29	[300, 20]	[0.33, 1.0]	[0.45, 1.4]	5.42×10^{-4}
	27.05 ± 0.27	[200, 1]	[0.33, 1.0]	[0.45, 0.8]	1.10×10^{-4}
Kaolinite@ $-19\,°$C	9.51 ± 0.16	[500, 90]	[0.45, 2.8]	[0.4, 0.6]	4.35×10^{-3}
	1.52 ± 0.06	[300, 20]	[0.45, 2.8]	[0.4, 0.5]	1.13×10^{-3}
	0.34 ± 0.03	[200, 8]	[0.45, 2.8]	[0.4, 0.5]	5.50×10^{-4}
	0.20 ± 0.02	[100, 15]	[0.45, 2.8]	[0.4, 0.55]	7.23×10^{-4}
	0.06 ± 0.01	[50, 5]	[0.45, 2.8]	[0.4, 0.8]	2.81×10^{-4}
Kaolinite@ $-25\,°$C	5.29 ± 0.12	[500, 90]	[0.4, 3]	[0.4, 0.6]	4.55×10^{-3}
	8.43 ± 0.15	[375, 60]	[0.45, 3]	[0.4, 0.6]	3.21×10^{-3}
	8.59 ± 0.15	[250, 40]	[0.5, 2.8]	[0.4, 0.65]	2.11×10^{-3}
	8.78 ± 0.15	[150, 25]	[0.45, 2.8]	[0.4, 0.8]	1.28×10^{-3}
	4.69 ± 0.11	[50, 15]	[0.45, 2.8]	[0.5, 0.8]	7.26×10^{-4}
Illite@ $-15\,°$C	1.59 ± 0.07	[1400, 15]	[0.28, 2.6]	[0.25, 0.5]	5.10×10^{-4}
	0.182 ± 0.02	[700, 5]	[0.27, 2.6]	[0.28, 1.3]	1.92×10^{-4}
	0.037 ± 0.01	[400, 2]	[0.27, 2.6]	[0.48, 0.5]	1.73×10^{-4}
	0.021 ± 0.03	[250, 3]	[0.27, 2.6]	[0.48, 2]	1.50×10^{-4}
Illite@ $-25\,°$C	8.04 ± 0.15	[1700, 25]	[0.28, 3]	[0.45, 0.5]	1.51×10^{-3}
	10.36 ± 0.17	[1500, 20]	[0.28, 3]	[0.45, 1]	1.27×10^{-3}
	10.92 ± 0.17	[800, 15]	[0.28, 3]	[0.45, 1.6]	7.14×10^{-4}

[a] Ice concentrations determined from particles greater than 20 µm as measured with the CDP for this experiment because the concentrations were high and hence the ice crystal sizes were small.

Table 2. Table showing results from dynamic light scattering experiments for the kaolinite sample.

	In water		
pH	diameter for 0.1 mg ml^{-1} (nm)	diameter for 0.33 mg ml^{-1} (nm)	diameter for 1 mg ml^{-1} (nm)
3.0	692.4	1143.0	1777.0
5.1	652.1	741.9	753.2
7.0	695.0	742.4	792.8
9.0	449.4	418.0	721.6
11.0	467.7	448.0	693.2
	100 mM NaCl		
pH	diameter for 0.1 mg ml^{-1} (nm)	diameter for 0.33 mg ml^{-1} (nm)	
3.0	1241.5	1585.0	
5.1	913.0	1318.5	
7.0	740.1	1533.5	
9.1	674.6	1350.0	
11.0	618.2	997.85	

Table 3. Table showing BET specific surface area of the different mineral samples used in this study.

Mineral sample	BET SSA $m^2 kg^{-1}$	Bulk density ($kg m^{-3}$)	SSA underestimation factor
Kaolinite	11 800	2650	~ 2.1
NX-Illite	104 200	2770	~ 19.2
K-feldspar	3115 [a]	2570	~ 0.53

[a] 3.5 times that of 890.

Table 4. Nomenclature.

|		
β	Coagulation kernel (m^3 particle^{-1} s^{-1})	Eq. (A1)
ϵ	Permittivity of water (F m^{-1})	Eq. (B4)
η_w	Viscosity of water $\sim 8.9 \times 10^{-4}$ Pa s	Eq. (A4)
κ	Reciprocal of Debye length (m^{-1})	Eq. (B2)
ν	The volume of a single particle in a bin (m^3)	Eq. (A1)
ζ_1	zeta potential of particle 1 (V)	Eq. (B1)
ζ_2	zeta potential of particle 2 (V)	Eq. (B1)
A_1, A_2	Hamaker constant for particles 1 and 2 (6.8×10^{-19} J)	Eq. (B5)
A_3	Hamaker constant for water (7×10^{-21} J)	Eq. (B5)
A_{132}	Hamaker constant for interaction between particle 1 and 2 in medium 3	Eq. (B5)
$D_{p,i}$	Particle diffusion coefficient (Stokes–Einstein coefficient) for bin i (m^2 s^{-1})	Eq. (A3)
e	Charge on electron ($\sim 1.6 \times 10^{-19}$ C)	Eq. (B4)
k_B	Boltzmann's constant, 1.381×10^{-23} m^2 kg s^{-2} K^{-1}	Eq. (A3)
m_i	Molar concentration of ions (mol m^{-3})	Eq. (B4)
N_A	Avogadros number (6.02×10^{23})	Eq. (B4)
N_B	The number of bins	Eq. (A2)
R_1	Radius of particle 1 (m)	Eq. (B1)
R_2	Radius of particle 2 (m)	Eq. (B1)
$r_{i,j}$	The radius of a particle in bin i or j (m)	Eq. (A3)
T	Temperature (K)	Eq. (B4)
u	Terminal velocity of particle in fluid (m s^{-1})	Eq. (A5)
V	The volume of the bin edges (m^3)	Eq. (A2)
n	The number concentration of a particle in a bin (m^{-3})	Eq. (A1)
v	The total volume all particles in a bin (m^3 m^{-3})	Eq. (A1)
V_A	van der Waals interaction potential (V)	Eq. (B5)
V_R	Interaction potential between two particles (V)	Eq. (B1)
V_T	Sum of all interaction potentials (V)	Eq. (C1)
W	Correction factor for particles interacting with potential	Eq. (C1)
Z	Valence of dissociation	Eq. (B4)
x	Distance between two particles (m)	Eq. (B2)
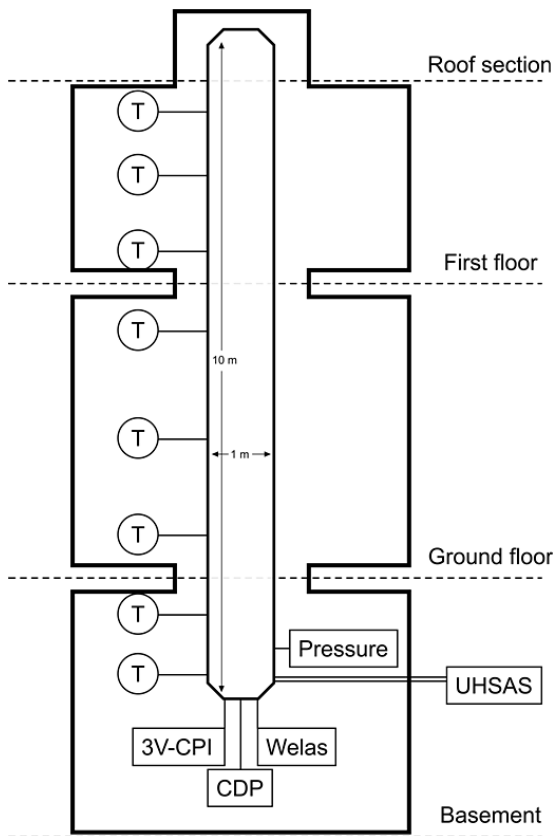
Figure 1. A schematic of the MICC cold-rooms and chamber. Outer lines mark the outline of the outer wall of the cold rooms, with the MICC tube inside. Temperature probes are labeled with a "T". Pressure, and cloud properties are monitor in the bottom section of the chamber.
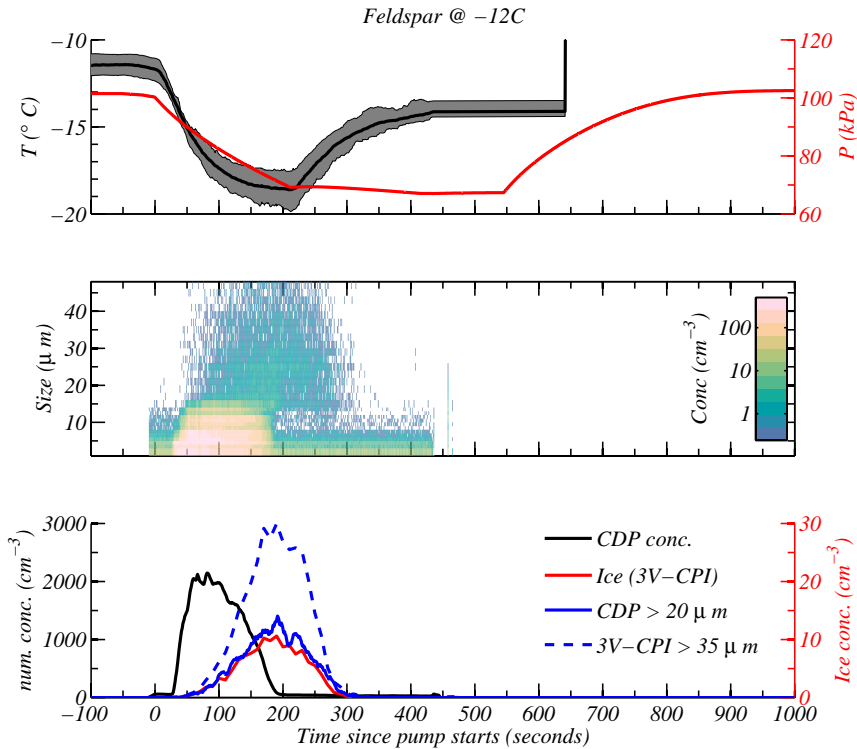
Figure 2. Feldspar mineral particles at $-12\,°C$. Top shows the temperature in the chamber (black line, left axis) and the pressure (red line, right axis). The black line is the mean of temperature probes, while the grey shading demarks the range in measured temperatures across all probes. Middle plot shows the size distribution as measured with the CDP instrument. Bottom plot shows: (1) the drop concentration measured with the CDP (black line, left axis); (2) the concentration of particles larger than the main droplet mode (solid blue line, right axis); (3) the ice crystal concentration measured with the 3V-CPI (red line, right axis); (4) the concentration of particles larger than 35 microns with the 3V-CPI (dotted blue, right axis).

32
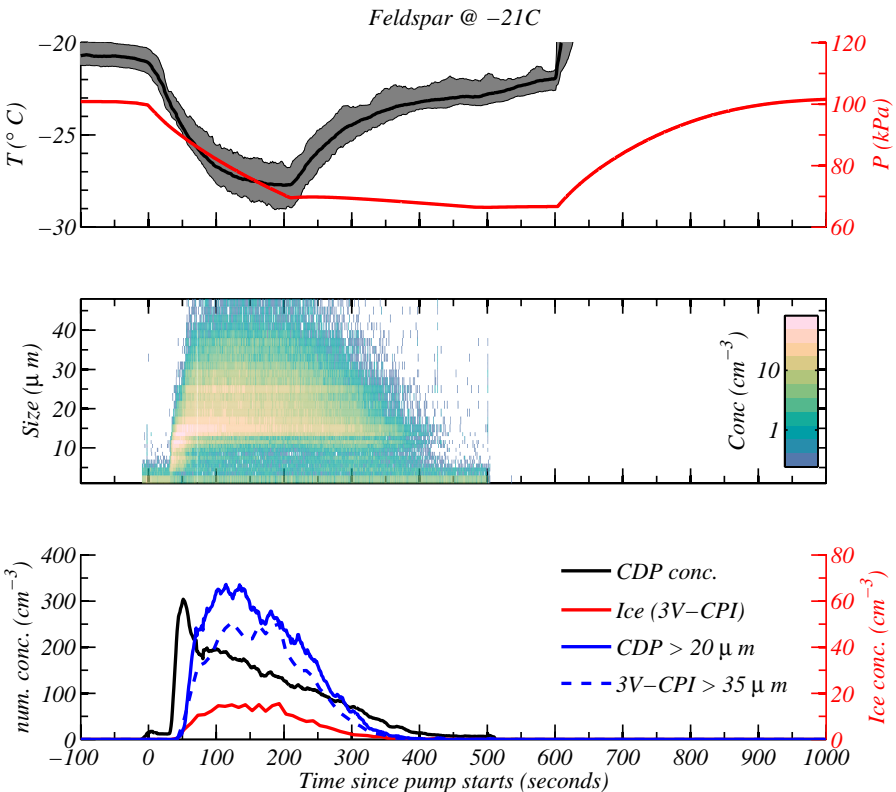
Figure 3. Same as Fig. 2, but for feldspar at $-21\,^\circ$C.
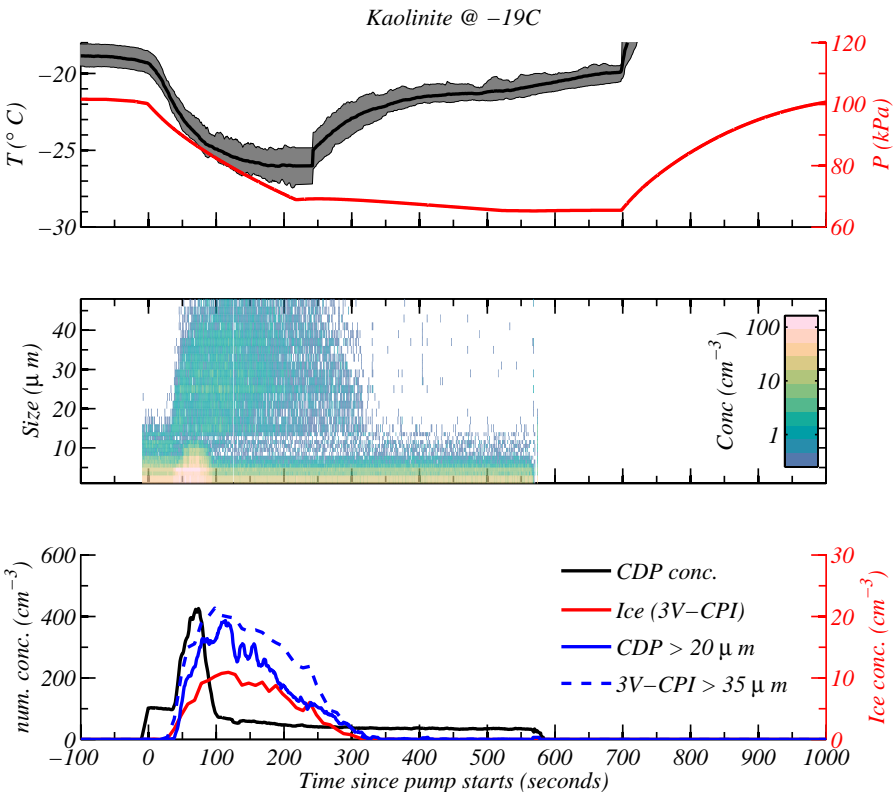
Figure 4. Same as Fig. 2, but for kaolinite at $-19\,°C$.
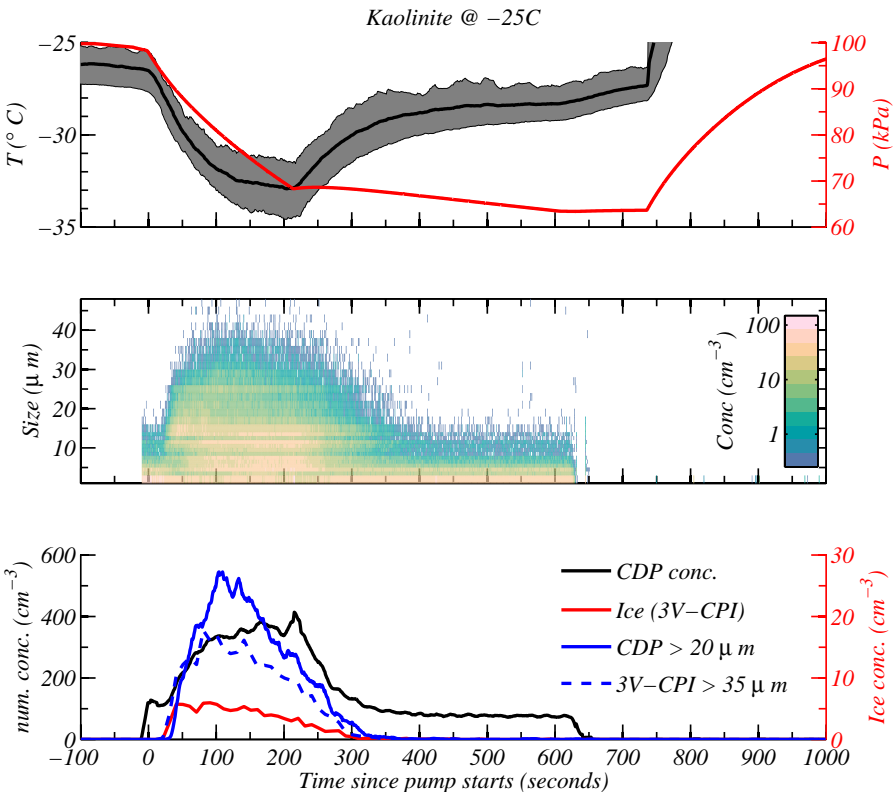
Figure 5. Same as Fig. 2, but for kaolinite at $-25\,^{\circ}\text{C}$.
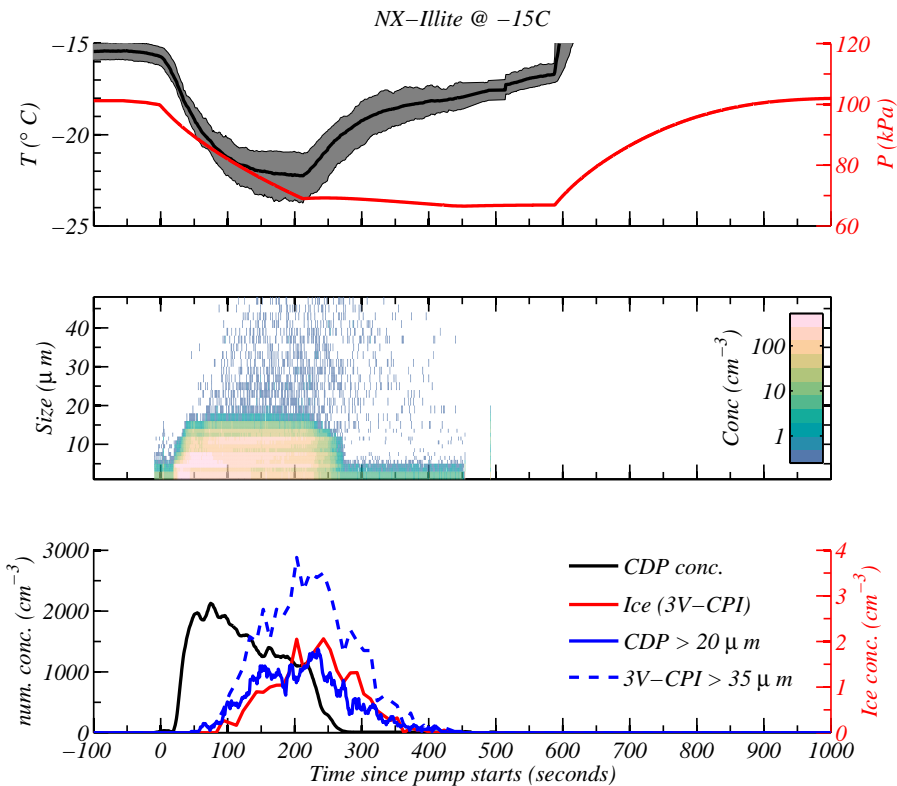
Figure 6. Same as Fig. 2, but for illite at −15 °C.
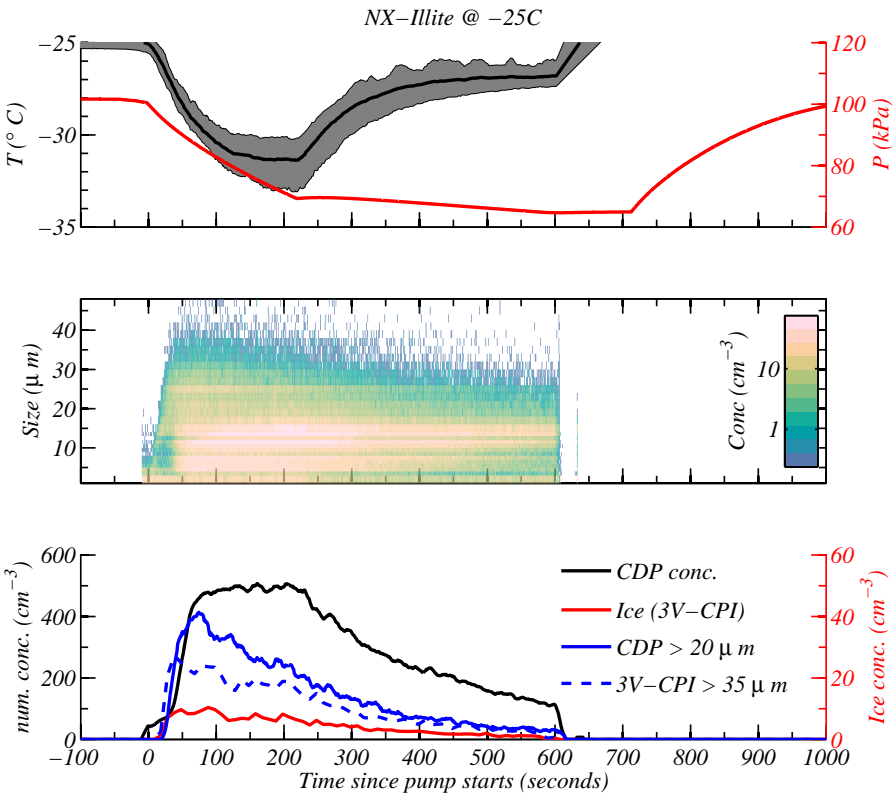
Figure 7. Same as Fig. 2, but for illite at −25 °C.
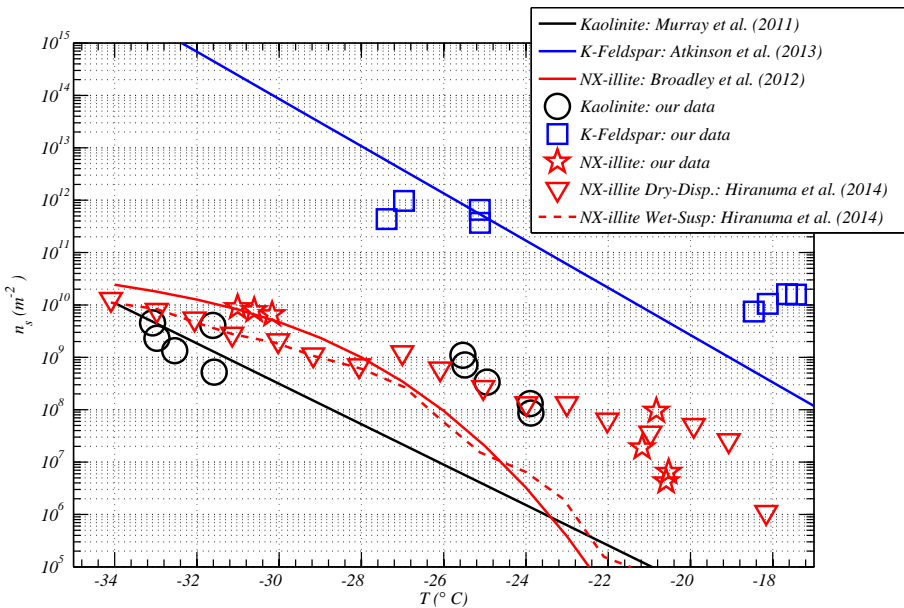
Figure 8. n_s values from the literature using wet-suspension methods are shown via the line plots: black line is for kaolinite from Murray et al. (2011); blue line is for K-feldspar from Atkinson et al. (2013); red solid line is for NX-illite from Broadley et al. (2012); red-dashed line is for NX-illite from Hiranuma et al. (2014). The open symbols correspond to n_s values derived using dry-dispersion: black circles are our data for Kaolinite; blue squares are our data for K-feldspar and stars are our data for NX-illite. Downward pointing triangles are for the NX-illite data derived using dry-dispersions from Hiranuma et al. (2014). For our data, measurement errors are typically the size of the symbols or less (see Table 1)

Figure 9. Figure summarising the results of the ACPIM simulations. The metric shown is the ratio of observed to modelled ice crystal number concentrations averaged over all expansions in a set of experiments. Error bars are 25th and 75th percentiles. The ACPIM model used the parametrisations from Murray et al. (2011); Broadley et al. (2012); Atkinson et al. (2013) for kaolinite, illite and K-feldspar particles respectively.
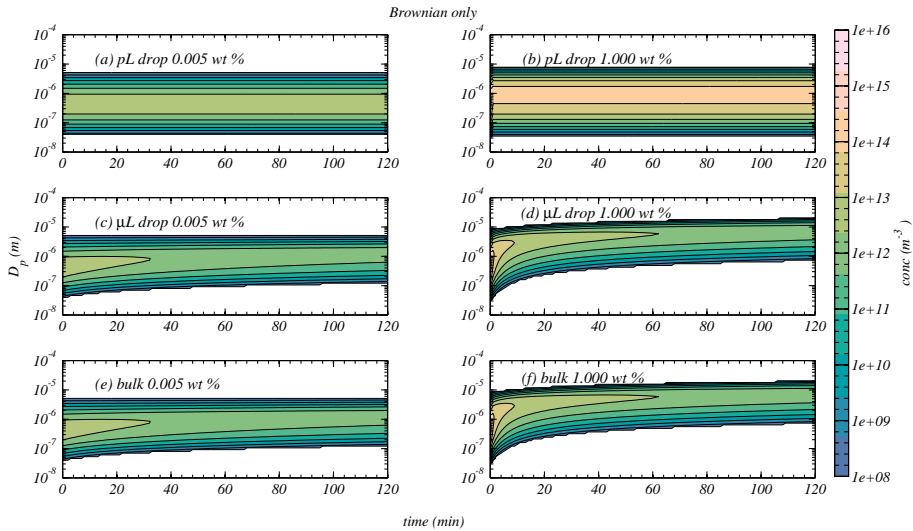
Figure 10. Numerical model simulations of the coagulation of mineral particles within suspension showing the size distribution evolution vs time. **(a)** is for a 0.005 wt % suspension inside a pico litre drop; **(b)** is the same as **(a)** but for 1.000 wt %; **(c)** is for a 0.005 wt % suspension inside a micro litre drop; **(d)** is the same as **(c)** but for 1.000 wt %; **(e)** and **(f)** are the same as **(c)** and **(d)** respectively, but for an infinite volume.
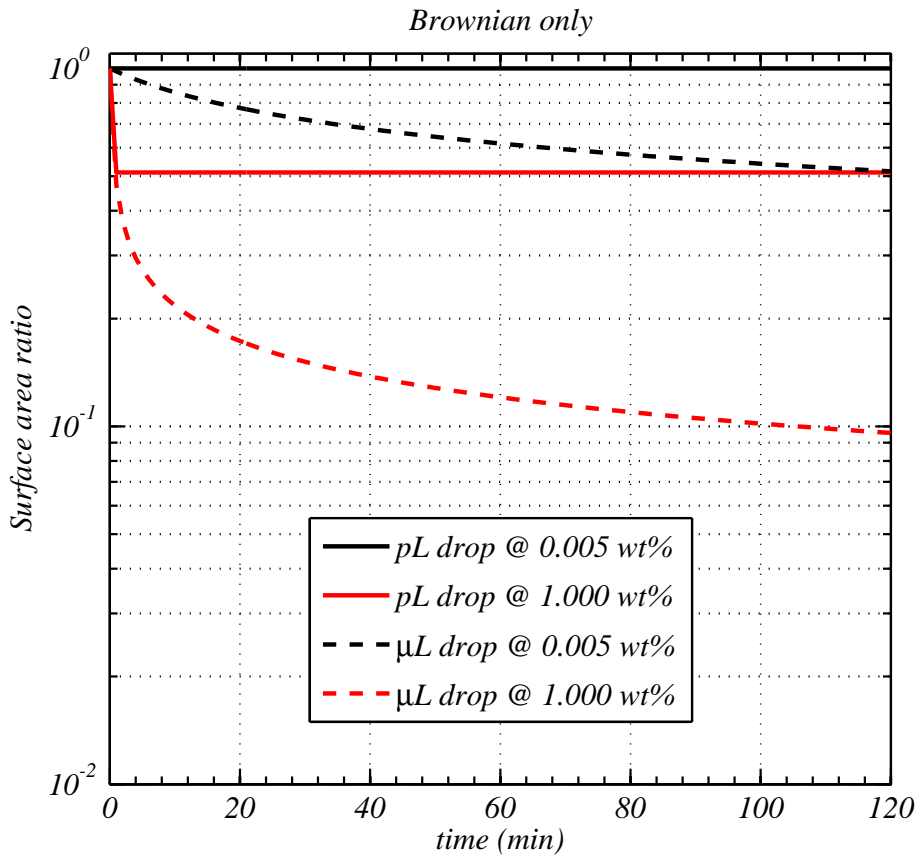
Figure 11. The evolution of the ratio of particle surface area to initial particle surface area for mineral particles undergoing coagulation in water suspension. The coagulation kernel assumed is that due to collisions arising from Brownian motion only.

41
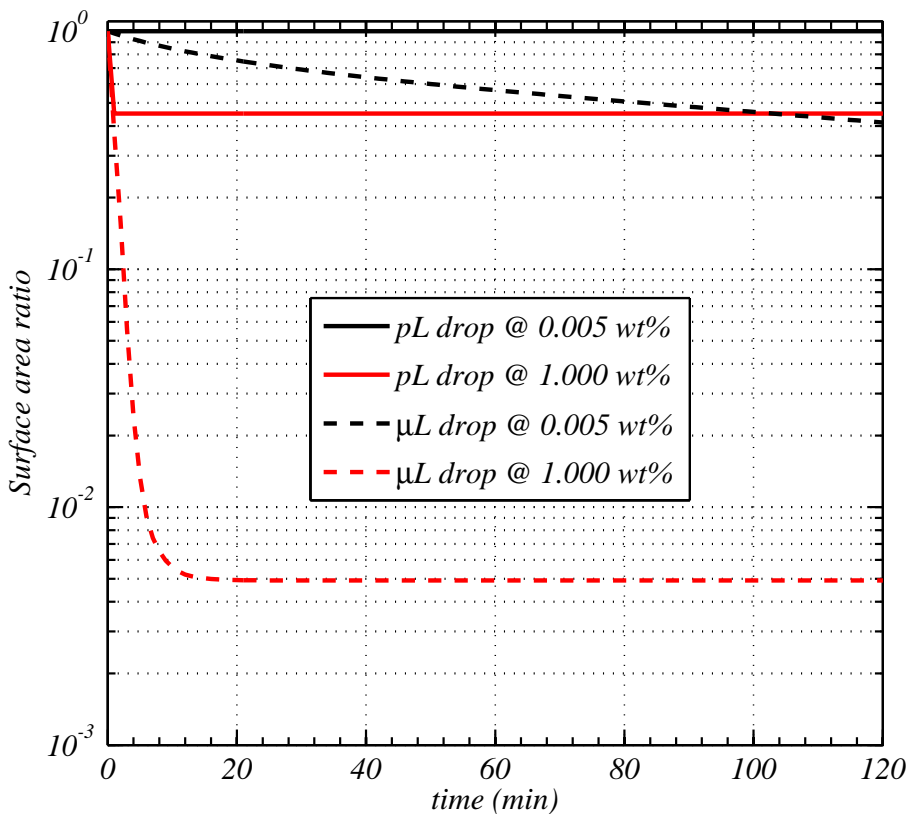
Figure 12. Same as Fig. 11, but with the coagulation due to Brownian motion and gravitational settling.
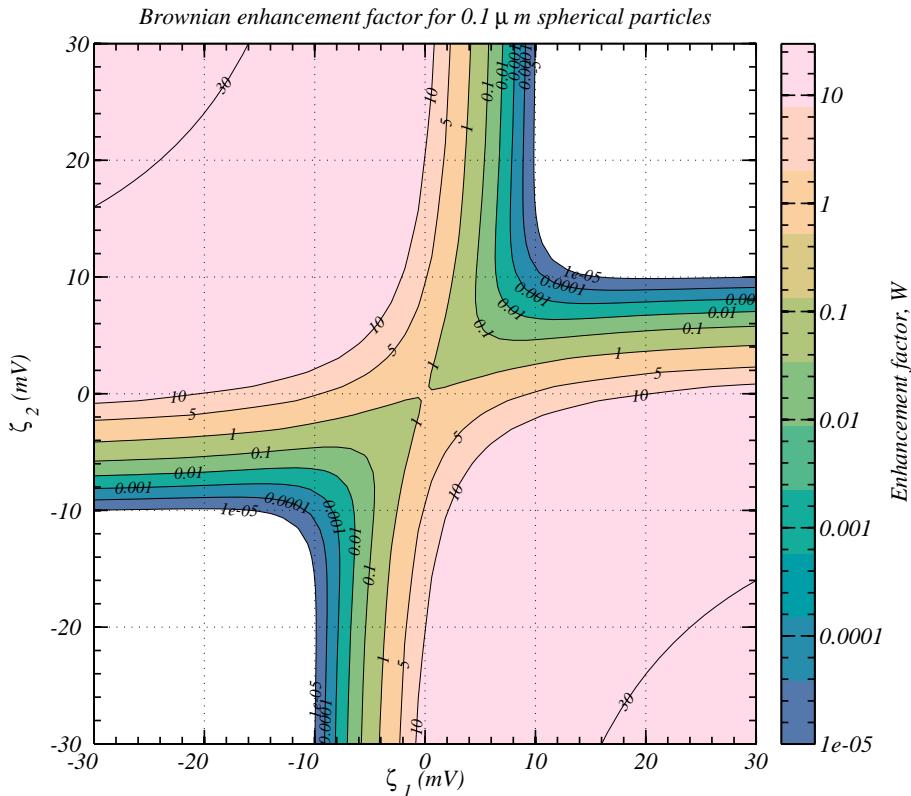
Figure 13. The enhancement factor of the Brownian collision kernel for two spherical particles in pure water as a function of the zeta-potential of both particles.